*Sound & Vibration* 2025, 59(5), 3662.
doi: https://doi.org/10.59400/sv3662

Article

# Creating a vibrational digital-twin of a Bell UH-1H helicopter tail-rotor blade for use in simulating centrifugal stiffening

**Daniel Winarski[1], Marc Lamparelli[2], Keith Landry[3], Tyson Winarski[4]**

[1] Independent Researcher, Tucson, AZ 85710, USA
[2] Spectral Dynamics, Inc., Troy, MI 48098, USA
[3] Independent Researcher, Savannah, GA 31405, USA
[4] Sandra Day O'Connor College of Law, Phoenix Campus, Arizona State University, Phoenix, AZ 85004, USA
*** Corresponding author:** Daniel Winarski, winarskifirm@gmail.com

**CITATION**

Winarski D, Lamparelli M, Landry K, et al. Creating a vibrational digital-twin of a Bell UH-1H helicopter tail-rotor blade for use in simulating centrifugal stiffening. Sound & Vibration. 2025; 59(5): 3662. https://doi.org/10.59400/sv3662

**ARTICLE INFO**

Received: 1 August 2025
Revised: 20 August 2025
Accepted: 1 September 2025
Available online: 12 September 2025



**Abstract:** Our objective was to study the centrifugal stiffening in the tail-rotor of a Bell UH-1H helicopter under operational rotation. Our method involved creating a digital-twin of the vibrations of a stationary model of this tail-rotor blade using empirical modal analysis, and STAR7 software from Spectral Dynamics to process 45 empirical frequency response functions. The results from the STAR7 modal analysis identified three out-of-plane flapping modes as well as a torsional mode of vibration. We assessed our digital-twin via the use of the Modal Assurance Criterion (MAC) as well as comparisons to analytical Euler-Bernoulli beam theory and ANSYS finite element analysis simulations. Then we augmented this stationary model to an operational rotating velocity of 173.2 rad/sec via use of the Structural Dynamics Modification (SDM) feature of STAR7 to enable quantification of the centrifugal stiffening of the tail-rotor across the blade's primary flapping and torsional modes. We concluded that the first flapping mode of vibration had the most centrifugal stiffening, and the succeeding modes experienced less stiffening as the modal frequency increased, which was consistent with modal energy being relatively constant across these modes. The digital twin approach demonstrated excellent agreement with analytical and numerical models, indicating its effectiveness for evaluating rotational stiffening in helicopter rotor components. Overall, the methodology demonstrated that empirical digital twin construction, combined with SDM techniques, provided a means of predicting the dynamic behavior of helicopter rotor components under rotation. This approach may serve as a foundation for applying artificial intelligence to rotorcraft diagnostics, structural health monitoring, and predictive maintenance.

**Keywords:** helicopter; tail-rotor blade; modal analysis; structural dynamics modification; centrifugal-stiffening; mode indicator function; modal assurance criterion; artificial intelligence

## 1. Introduction

The Bell UH-1 [1], nicknamed "Huey", was the beginning of a family of utility helicopters designed and produced by the American aerospace company Bell Helicopter. **Figure 1** shows a Bell UH-1H along with the XYZ coordinate system used to create a digital-twin of its tail-rotor blade, which rotated about the Z-axis when the helicopter was in flight. This digital-twin was used study the centrifugal stiffening of the first four modes of vibration, via structural dynamics modification.


**Figure 1.** Bell UH-1H [2] showing our XYZ Coordinate System.

Guivarch, et-al., [3] created helicopter dynamic systems digital-twin using multibody simulation and Li, et-al., [4] provided an introduction to digital-twins. Our study was limited to a component digital-twin, specifically of the tail-rotor. Santos, et-al., [5] and Grappasonni, et-al., [6] quantified their results via Modal Assurance Criterion diagrams, which influenced our use of the same. Rizo-Patron and Sirohi [7] studied the theoretical and empirical modal analysis of the first three out-of-plane flapping modes of a beam simulating a helicopter rotor, using digital image correlation as the beam rotated at 0, 300, 600, and 900 RPM. Due to expermimental error, slight centrifugal weakening was inadveretently detected at 900 RPM in part because the centrifugal stiffening at this higher mode was so small. The Rizo-Patron theoretical model included a centrifugal-stiffening term which involved mass per unit length and the square of Ω, the speed of rotation, which led to our using the same.

Our study benefited from previous studies [3–7] as we constructed a digital-twin of the vibrations of a stationary model of a helicopter tail-rotor blade using empirical modal analysis and STAR7 software from Spectral Dynamics to process the empirical modal analysis. We assessed our digital-twin via the use of the Modal Assurance Criterion as well as comparisons to theoretical beams and ANSYS finite element analysis. Then we augmented this stationary model to an operational rotating velocity via use of the Structural Dynamics Modification feature of STAR7 to quantify centrifugal stiffening of the tail-rotor. Pima Air and Space Museum has these tail-rotor blades on display [8].

## 2. Materials and methods

The tail-rotor of the UH-1H helicopter had two blades. The radius R of the arc of the tail-rotor was 1.295 m (4.25 feet). Its operational angular velocity was $\Omega_z$ = 173.2 radians/second (1654 RPM) about the horizontal Z-Axis. The Y-Axis chord of the largely rectangular blade was 213.6 mm (8.41 inches). The mass of the one blade was approximately 3 kg and the overall blade length along the X-Axis was L = 1.16 m. The center of mass was located 0.685 m from the outer edge, 0.475 m from the inner

edge of the blade. Two mount holes, 30 mm from the root end of the blade, were used to cantilever the tail-rotor blade from a steel channel, as shown in **Figure 2**.

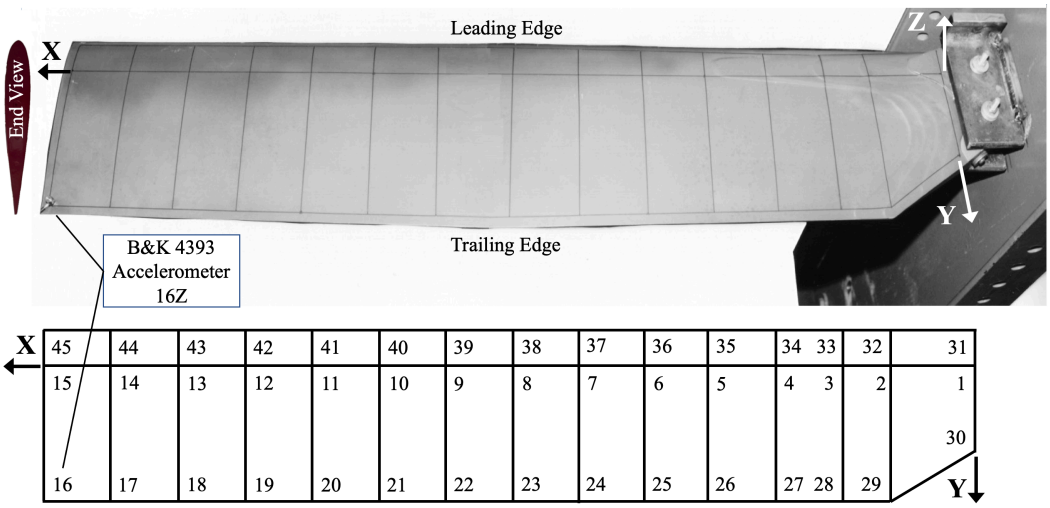


**Figure 2.** Layout of 45 Nodes along the Top Surface of the UH-1H Tail-Rotor Blade.

**Figure 2** shows the layout of 45 nodes along the top surface of the UH-1H tail-rotor blade, which is effectively a fixed-free cantilever beam. Santos, et-al., [5] used 55 nodes to study a main rotor of a helicopter, each having an accelerometer. In our study, a single Brüel & Kjær (B&K) 4393 accelerometer (fixed-location response, in $m/s^2$) [9] was mounted at the radially outermost node along the trailing edge of the tail-rotor blade (node 16), **Figure 2**, with beeswax. It was felt that measuring the system response at this node would afford the maximum sensitivity to both flapping and torsion and would not be a vibrational node (point of zero amplitude for any of the modal resonances).

As shown in **Figure 3**, a B&K 8202 impact hammer and 8200 force transducer (excitation, in Newtons) [10] were used to gently tap the 45 nodes, and the fixed location accelerometer sensed the subsequent response. Using the hard-rubber tip, without the additional mass, on the impact hammer limited the excitation to 500 Hz, coinciding nicely with the 400 Hz bandwidth on the B&K 2034 signal analyzer. B&K 2644 line-driver charge-amplifiers [11] amplified the low-level signals from the accelerometer and force transducer before these signals were received by the signal analyzer. The outputs of the signal analyzer were 45 Frequency Response Functions (*.FRF). Structural Measurements System (SMS) StarStruct software originally performed the calculation of mode shapes, modal frequency and modal damping ratios, similar to that described by Winarski [12].

**Table 1** lists the XYZ coordinates of the 45 nodes comprising the helicopter tail-rotor blade. The nodes were numbered starting along the thickest portion of the blade, then along the trailing edge of the blade, then finally along the leading edge of the blade.

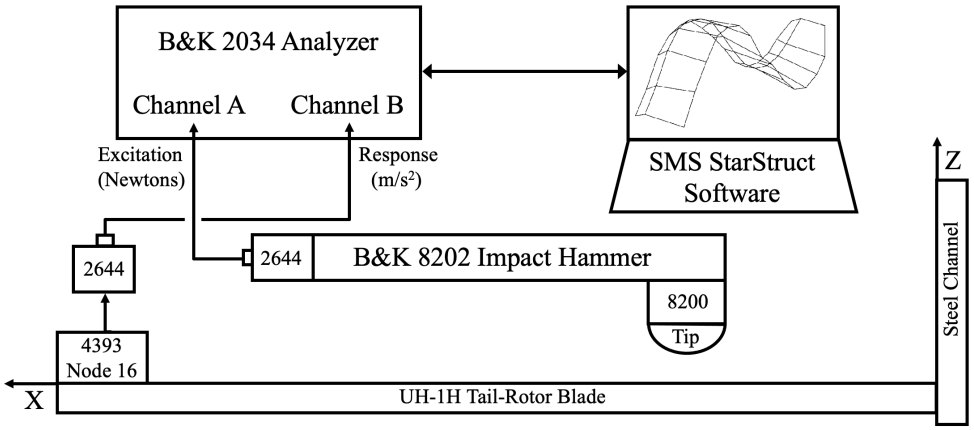


**Figure 3.** Diagram of Experimental Setup for Gathering Frequency Response Functions.

**Table 1.** 45 STAR7 Modal Nodes comprising the Helicopter Tail-Rotor Blade.

| STAR7 node | X (m) | Y (m) | Z (m) | Rotor blade component | STAR7 Node | X (m) | Y (m) | Z (m) | Rotor blade component |
|---|---|---|---|---|---|---|---|---|---|
| 1 | 0 | 0 | 0.016 | Max Thick | 2 | 0.100 | 0 | 0.016 | Max Thick |
| 3 | 0.155 | 0 | 0.016 | Max Thick | 4 | 0.230 | 0 | 0.016 | Max Thick |
| 5 | 0.310 | 0 | 0.016 | Max Thick | 6 | 0.385 | 0 | 0.016 | Max Thick |
| 7 | 0.460 | 0 | 0.016 | Max Thick | 8 | 0.535 | 0 | 0.016 | Max Thick |
| 9 | 0.613 | 0 | 0.016 | Max Thick | 10 | 0.689 | 0 | 0.016 | Max Thick |
| 11 | 0.765 | 0 | 0.016 | Max Thick | 12 | 0.841 | 0 | 0.016 | Max Thick |
| 13 | 0.917 | 0 | 0.016 | Max Thick | 14 | 0.995 | 0 | 0.016 | Max Thick |
| 15 | 1.070 | 0 | 0.016 | Max Thick | 16 | 1.070 | 0.160 | 0 | B&K 4393 |
| 17 | 0.995 | 0.160 | 0 | Trailing | 18 | 0.917 | 0.160 | 0 | Trailing |
| 19 | 0.841 | 0.160 | 0 | Trailing | 20 | 0.765 | 0.160 | 0 | Trailing |
| 21 | 0.689 | 0.160 | 0 | Trailing | 22 | 0.613 | 0.160 | 0 | Trailing |
| 23 | 0.535 | 0.160 | 0 | Trailing | 24 | 0.460 | 0.160 | 0 | Trailing |
| 25 | 0.385 | 0.160 | 0 | Trailing | 26 | 0.310 | 0.160 | 0 | Trailing |
| 27 | 0.230 | 0.160 | 0 | Trailing | 28 | 0.155 | 0.160 | 0 | Trailing |
| 29 | 0.100 | 0.160 | 0 | Trailing | 30 | 0 | 0.100 | 0 | Trailing |
| 31 | 0 | −0.040 | 0 | Leading | 32 | 0.100 | −0.040 | 0 | Leading |
| 33 | 0.155 | −0.040 | 0 | Leading | 34 | 0.230 | −0.040 | 0 | Leading |
| 35 | 0.310 | −0.040 | 0 | Leading | 36 | 0.385 | −0.040 | 0 | Leading |
| 37 | 0.460 | −0.040 | 0 | Leading | 38 | 0.535 | −0.040 | 0 | Leading |
| 39 | 0.613 | −0.040 | 0 | Leading | 40 | 0.689 | −0.040 | 0 | Leading |
| 41 | 0.765 | −0.040 | 0 | Leading | 42 | 0.841 | −0.040 | 0 | Leading |
| 43 | 0.917 | −0.040 | 0 | Leading | 44 | 0.995 | −0.040 | 0 | Leading |
| 45 | 1.070 | −0.040 | 0 | Leading | | | | | |

The SMS StarStruct software was then replaced by its most recent successor, Spectral Dynamics STAR7 Premier Modal software 3410–9710 [13], to take advantage of greatly improved post-processing graphics and analysis capabilities. The transfer of modal results from the old SMS StarStruct package to the new Spectral Dynamics STAR7 package began with creating a workspace then creating a project within that workspace. Once inside that project, as shown in **Figure 4**, right click on MODEL > IMPORT and select STAR v5 Coordinate Tables (*.CRD), navigate to the desired SMS *.CRD file and upload it, to produce the basic geometry of the modal analysis. Next, right click on MEASUREMENT DATA > IMPORT and select STAR v5 Measurements,

navigate to the desired SMS *.FRF files, select all using shift-click, and upload them. Lastly, open PARAMETERS and select the units of SI HZ, Excitation in Newtons for the impact hammer and force transducer, and Response in $m/s^2$ for the accelerometer. Under acquisition setup, Fixed Response was selected, and the master reference was 16Z as the accelerometer was at node 16 in the Z direction. Using the FILE menu, the project was then saved as a new *.PRJ file in the respective *.SWS workspace file, resulting in the model being saved to a new *.CMM file and the measurements being saved to a new *.SDD file.

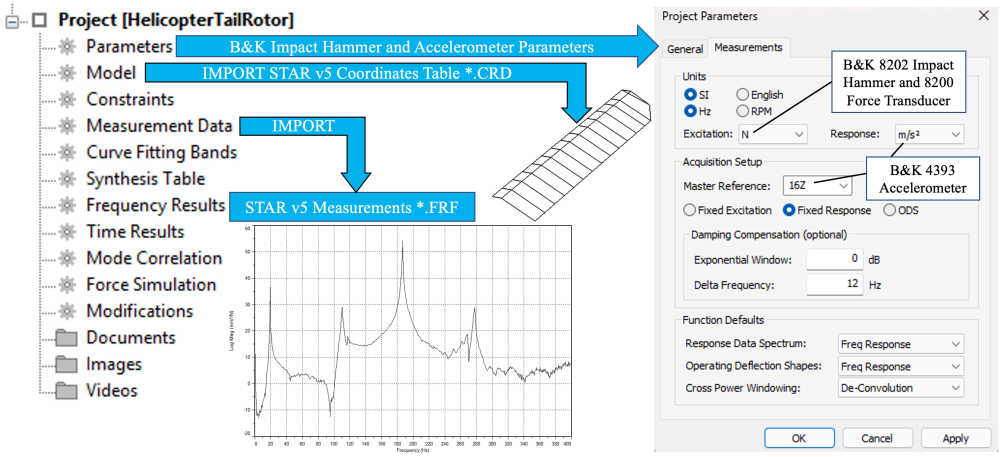


**Figure 4.** Transfer of old SMS StarStruct data to the new Structural Dynamics STAR7.

## 3. Results

This section shows our use of the STAR7 Mode Indicator Function and Advanced Curve Fitter to identify three flapping and one torsional mode of vibration.

### 3.1. Identifying modes of vibration using STAR7

**Figure 5** shows the exemplary 45Z–16Z Frequency Response Function displaying four potential modes of vibration over the frequency range of $0 \leq \omega \leq 400$ Hz. 45Z–16Z meant that this was the response at node 45Z with the reference at 16Z, the location of the accelerometer. 45Z was picked as the exemplary response because it was at the outer extremity of the rotor and at the leading edge of the rotor blade. With the accelerometer at the outer extremity of the rotor and at the trailing edge of the rotor blade, it was felt that the 45Z–16Z pair gave the best representation of both the flapping modes and torsional mode of vibration of the tail-rotor blade.

The mode identification using the Advanced Curve Fitter (ACF) method began by selecting Analysis from the top tool bar, then selecting Mode Indicators for all 45 nodes. The Mode Indicator Function (MIF) was used to locate the modal (resonance) peaks for our tail-rotor. This MIF function summed, by a stable averaging method, all of the measurements in a user-prescribed DOF selection and accumulated a Modal Peaks function in a data block which was then displayed as shown in **Figure 6**.

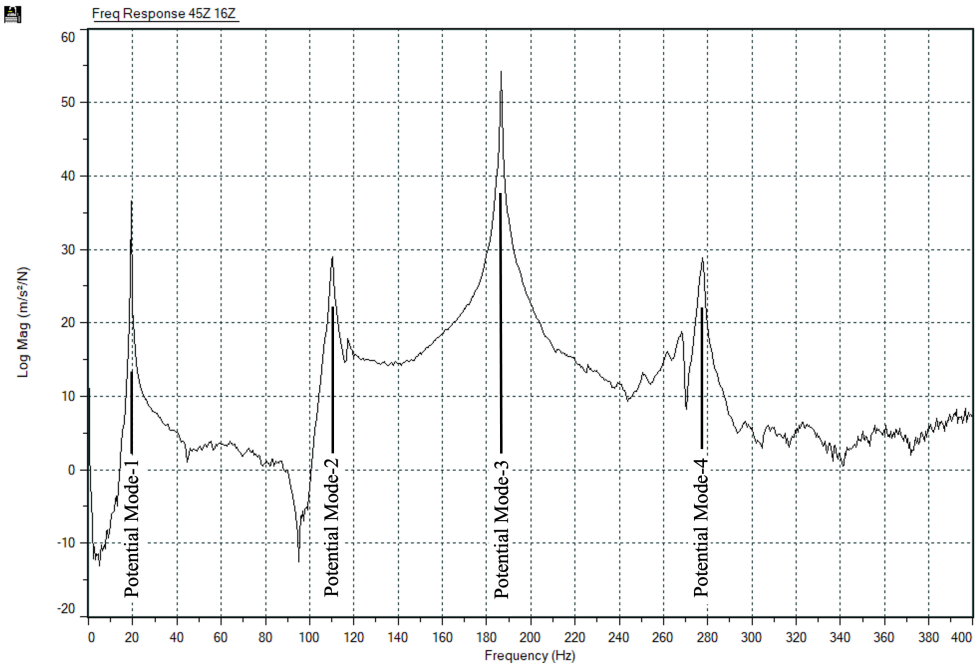


**Figure 5.** 45Z–16Z Frequency Response Function displaying four potential modes.

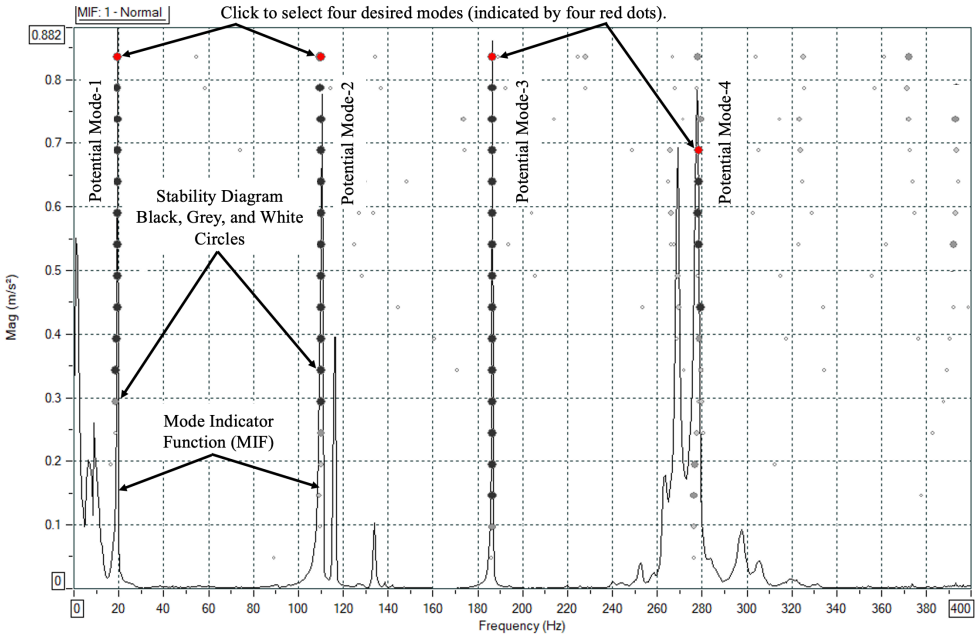


**Figure 6.** Advanced Curve Fitter with Mode Indicator Function and Stability Diagram.

Next, the Stability Diagram icon was selected, to superimpose the circles of the Stability Diagram upon the Mode Indicator Function in **Figure 6**. From the Estimate F&D tab, the Model Size of 4 to 20 was selected, then Calculate was selected. If a potential mode was found, the Stability Diagram reported an open circle. If the same mode was stable within the user-selected frequency tolerance, a light gray circle was reported. If both the difference in frequency and damping values were within tolerance, the new circle was shaded gray. If both the difference in frequency and damping values continued to be in tolerance, the new circle was black. The stabilization diagram in **Figure 6** is part of the STAR Poly-Reference Curve Fitter. In **Figure 6**, only one Reference was used. The stability diagram is based on the Least Square

Complex Exponential (LSCE) technique which is a time domain technique utilizing the IFFT (Inverse Fast Fourier Transform) of the selected FRFs The stability diagram was overlaid with the Mode Indicator Function (MIF) to highlight potential modes. The MIF function in **Figure 6** was 1-Normal, where the Normal function was the average of the real portion of the FRFs divided by the average of the FRF Magnitudes. Using 1-Normal produced peaks at potential modes, whereas the alternative Normal function produced minimums at potential modes of vibration.

The Estimate F&D option was used to automatically extract the frequency and damping values of resonances for a model size within a set bandwidth. Solving for the frequency and damping (F&D) values for a particular model size involves finding the roots (poles) of a characteristic equation, the order of which is twice the model size being analyzed. The roots of this equation are the F&D values for which the equation is being solved. After all the roots for a particular model size are calculated, they are tested to see if they represent potential modes of vibration. The Advanced Curve Fitting algorithm makes certain assumptions about the structure being investigated: that it is a linear system, that it is a second-order system and that it displays Maxwell's reciprocity. Under these assumptions, the roots of the characteristic equation for a true mode of vibration must appear in complex conjugate pairs. Any of the calculated roots that do not satisfy this condition are eliminated from the list of potential modes for the current model size. The roots (poles) that are complex conjugate pairs are tested further to make sure that the frequency value of the root (its imaginary part) is within the specified analysis frequency range. Roots not satisfying this condition are also eliminated from the potential mode list for the current model size.

A progression of dark grey circles followed by black circles was clearly evident in **Figure 6**. In order to calculate the four mode shapes seen in **Figures 7** and **8**, each mode had to be selected by clicking on one of the circles, as shown by the four red circles, then selecting Analysis > Curve Fitting > Poly-Reference and clicking on Fit All. Poly-Reference took the modes identified by the manually-selected red dots in the stability diagram and calculated the resulting mode shapes shown in **Figures 7** and **8**, based amplitude and phase in the frequency response data. With the Complex Shape option in Poly-Reference, the equations assume the most general form for the FRFs. With the general form of the FRFs, the computed residues (from which the mode shapes are derived) are complex, and will result in complex modes. The Residual Mass compensation accounts for the influence of modes lower than the analysis band; and the Residual Flexibility compensates for modes above the analysis band.

## 3.2. Identifying modes of vibration using STAR7 and ANSYS

**Figure 7** shows the identified flapping modes 1, 2, and 4 from the perspective of the X-Z plane, which best differentiates between the three distinctive mode shapes for a nonrotating tail-rotor blade, $\Omega_z = 0$.

The flapping modes "a-c" were identified via STAR7 ACF modal analysis and the corresponding flapping modes "d-f" were identified via ANSYS 2025R2 [14] finite element analysis. The colorization of flapping modes "d-f" went from red denoting maximum displacement to blue denoting zero displacement.

**Figure 8** then shows an isometric view of torsional mode-3, to better visualize the rotational-deflection of the nonrotating tail-rotor blade about the X-axis. The torsional mode "a" was identified via STAR7 ACF modal analysis and the corresponding torsional mode identified "b" was via ANSYS 2025R2 finite element analysis.

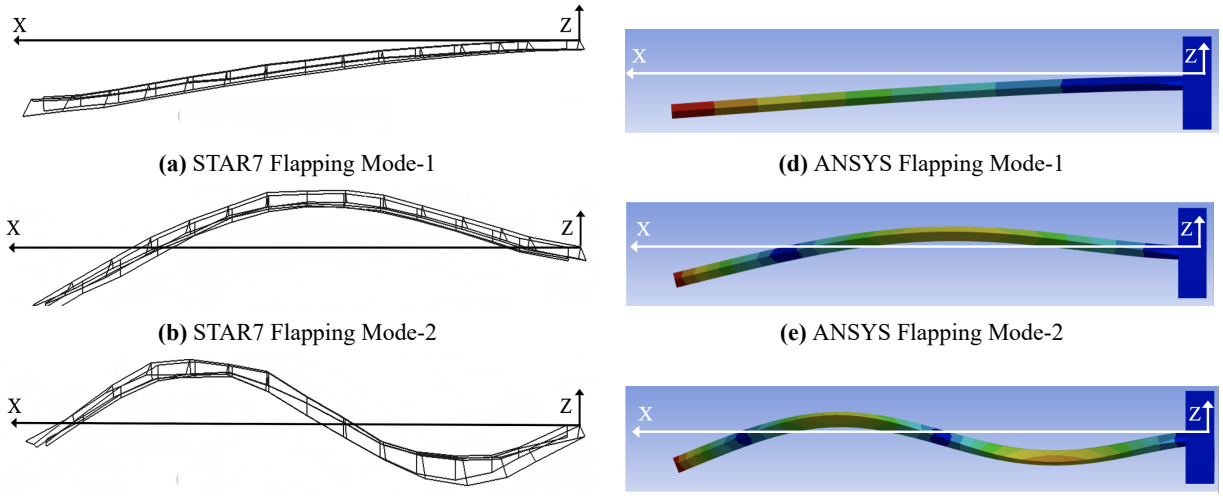


**(a)** STAR7 Flapping Mode-1 **(d)** ANSYS Flapping Mode-1

**(b)** STAR7 Flapping Mode-2 **(e)** ANSYS Flapping Mode-2

**(c)** STAR7 Flapping Mode-4 **(f)** ANSYS Flapping Mode-4

**Figure 7.** Flapping Modes 1, 2 and 4, STAR7 ACF and ANSYS Finite Element, $\Omega_z = 0$.

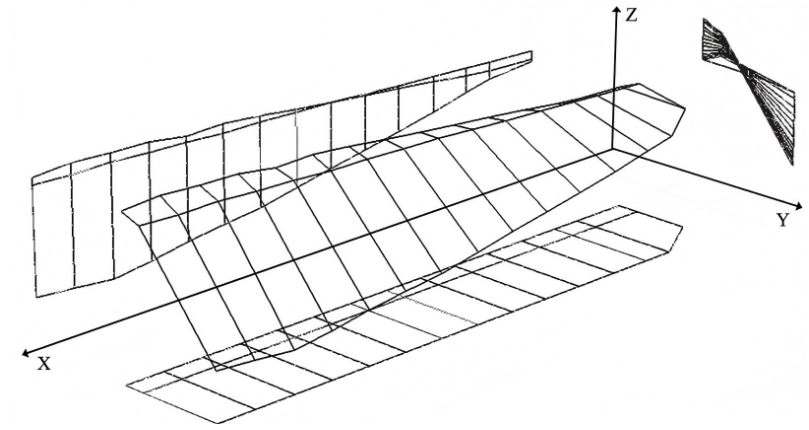


**(a)** STAR7 Torsion Mode-3

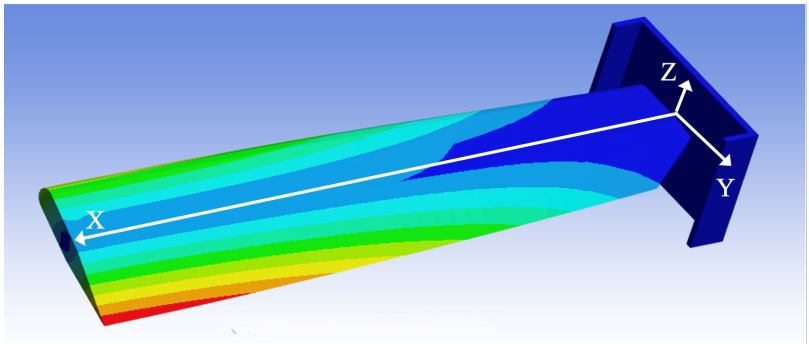


**(b)** ANSYS Torsion Mode-3

**Figure 8.** Torsion Mode-3 using the STAR7 ACF and ANSYS Finite Element, $\Omega_z = 0$.

## 4. Discussion

The flapping modes and torsional mode from **Figure 7a–c** and **Figure 8a** are summarized in **Table 2**, where the modes are numbered in order of frequency. The

frequencies and damping determined via STAR7 for separate tests were averaged and the respective spreads calculated.

**Table 2.** STAR7 Average Modal Frequencies, Damping, and Spread, for $\Omega_z = 0$.

| STAR7 mode number | STAR7 mode type | Average frequency ω | Average damping ζ | Frequency spread ω | Damping spread ζ |
|---|---|---|---|---|---|
| 1 | Flapping | 19.32 Hz | 1.43 % | ± 0.01 Hz | ± 0.08 % |
| 2 | Flapping | 109.88 Hz | 3.02 % | ± 0.47 Hz | ± 2.14 % |
| 3 | Torsion | 186.40 Hz | 0.20 % | ± 0.04 Hz | ± 0.01 % |
| 4 | Flapping | 278.12 Hz | 0.62 % | ± 0.28 Hz | ± 0.02 % |

**Table 3** lists the empirical frequency ratios in column 3 for the three STAR7 flapping frequencies in column 2, from **Table 2**. The ratio of 5.68:1 was calculated from the quotient 109.78/19.32, and the ratio of 14.39:1 was calculated from the quotient 278.11/19.32.

**Table 3.** Comparing STAR7 and ANSYS Flapping Frequencies, for $\Omega_z = 0$.

| STAR7 flapping mode | STAR7 frequency average ω | STAR7 frequency ratio | Blevins [15] Lima [16] ratio | Yoo [17] Wright [18] ratio | ANSYS frequency Ω | ANSYS Frequency Ratio |
|---|---|---|---|---|---|---|
| 1 (**Table 2**) | 19.32 Hz | 1:1 | 1:1 | 1:1 | 19.182 Hz | 1:1 |
| 2 (**Table 2**) | 109.88 Hz | 5.68:1 | 6.267: 1 | 6.267:1 | 120.02 Hz | 6.256:1 |
| 4 (**Table 2**) | 278.12 Hz | 14.39:1 | 17.547:1 | | 335.03 Hz | 17.467:1 |

In column 4 of **Table 3**, the corresponding theoretical frequency ratios were listed from Blevins [15] and Lima [16], for an Euler-Bernoulli beam of uniform cross-section. In column 4, the ratio of 6.267:1 was calculated from $(\lambda_2/\lambda_1)^2$, where $\lambda_2 = 4.69409113$ and $\lambda_1 = 1.87510407$. Similarly, the ratio of 17.547:1 was calculated from $(\lambda_3/\lambda_1)^2$, where $\lambda_3 = 7.85475744$.

In columns 5 of **Table 3**, the corresponding theoretical frequency ratios were listed from Yoo and Shin [17], and Wright, et-al., [18], respectively. Columns 4–5 indicated a reasonable agreement between the published Euler-Bernoulli theory and the experimental results from the tail-rotor blade using STAR7, as tabulated in column 3. The EXCEL = PEARSON correlation between the STAR7 frequency ratios in column 3 of **Table 3** and the Blevins and Lima frequency ratios in column 4 was 99.9%, indicating a very strong correlation between our stationary tail rotor blade and a stationary Euler-Bernoulli beam.

The ANSYS finite element frequencies, column 6, and ratios, column 7, agreed closely with Blevins [15] and Lima [16].

## 4.1. STAR7 and ANSYS modal assurance criterion, $\Omega_z = 0$

In **Figure 9**, the 3-D histogram (left) and 2-D table (right) Modal Assurance Criterion [19] for the STAR7 Advanced Curve Fitter are displayed for the four modes of vibration of interest shown in **Figures 7** and **8**, at $\Omega_z = 0$. Pastor, et-al., [20] was particularly helpful in understanding **Figure 9**. The mathematics of the Modal Assurance Criterion as discussed by Greś [21], Allemang [22], Samman [23], Brehm, et-al., [24], and Fotsch, et-al., [25] also provided useful insight to the Modal Assurance

Criterion. In **Figure 9**, the MAC is a symmetric 4-by-4 matrix calculated by the pair-wise dot product of eigenvectors of the four subject modes. The comparison values for each pair of modes varied between 0 and unity (100%). The main-diagonals in **Figure 9** represented a form of autocorrelation and all were unity, as expected. A form of cross-correlation is shown for half of the off-diagonal elements (6 total) is depicted via a histogram then tabulated for all off-diagonal elements (12 total). The color coding for **Figure 9** was as follows: purple represented a value between 0.90 (90%) and 1.00 (100%) as used for the main-diagonal values, burnt-orange represented a value between 0.50 (50%) and 0.90 (90%), pink represented a value between 0.02 (2%) and 0.50 (50%) as used for several off-diagonal values, and yellow-lime represented a value between 0 (0%) and 0.02 (2%) as used for several off-diagonal values. The low off-diagonal values in **Figure 9** indicated a high degree of orthogonality between modes 1–4, as desired.

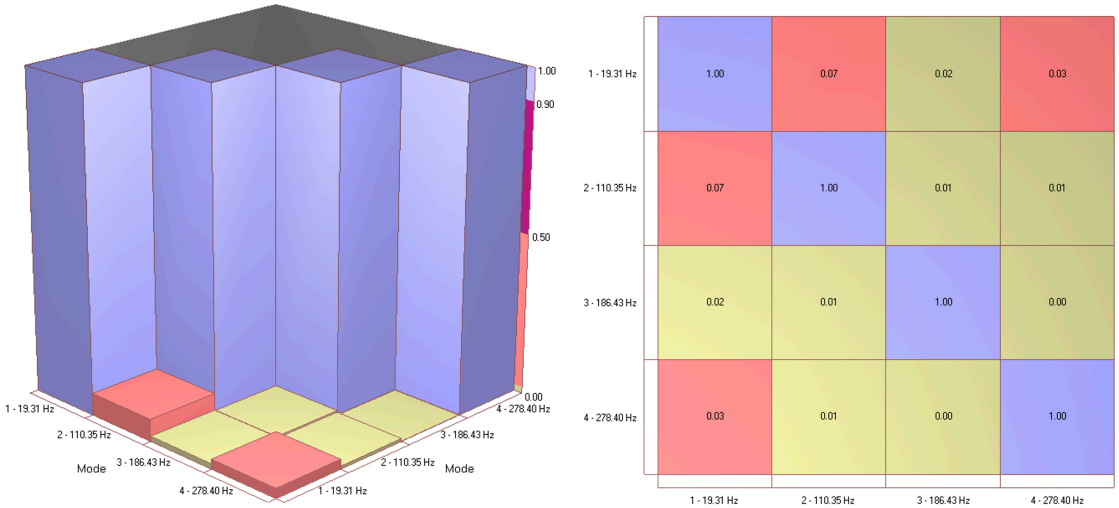


**Figure 9.** 3-D histogram (left) and 2-D table (right) STAR7 MAC, $\Omega_Z = 0$.

In **Figure 10**, the 3-D histogram (left) and 2-D table (right) Modal Assurance Criterion [14] for the ANSYS 2025R2 finite element model are displayed for the four modes of vibration of interest shown in **Figures 7** and **8**, at $\Omega_Z = 0$. In **Figure 10**, as in **Figure 9**, the MAC was a symmetric 4-by-4 matrix calculated by the pair-wise dot product of eigenvectors of the four subject modes. The comparison values for each pair of finite element modes was either 0 (blue) or unity (red). The main-diagonals in **Figure 10** represented a form of autocorrelation and all were unity, as expected. A form of cross-correlation is shown for half of the off-diagonal elements (6 total) is depicted via a histogram then tabulated for all off-diagonal elements (12 total). The zero values in **Figure 10** indicated a high degree of orthogonality between modes 1–4, as desired.

Calculating the ANSYS Modal Assurance Criterion in **Figure 10** was not intuitive. The ANSYS MAC calculator required specifying the location of the mode eigenvectors in the following subdirectory: C:\ANSYS_WB\Project\dp0\SYS\MECH\file.rst.

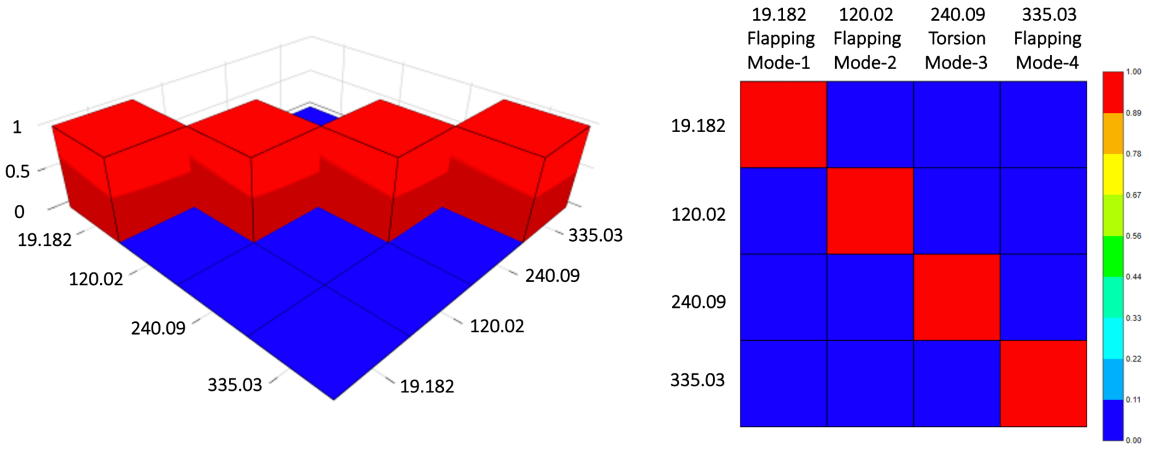


**Figure 10.** 3-D histogram (left) and 2-D table (right) ANSYS 2025R2 MAC, $\Omega_z = 0$.

## 4.2. STAR7 structural dynamics modification, $\Omega_z = 173.2$ rad/sec

The STAR7 DOF-to-ground structural dynamics modification [13] was chosen to add stiffness to the tail-rotor blade. This simulated the centrifugal-stiffening caused by the rotation of the blade when in operation at $\Omega_z = 173.2$ rad/sec (1,652 RPM), **Table 4**.

**Table 4.** STAR7 Structural Dynamics Modification Table, $\Omega_z = 173.2$ rad/sec.

| Row | Enable | Type | Amount | DOF/Point 1 | DOF/Point 2 | Ground X | Ground Y | Ground Z |
|---|---|---|---|---|---|---|---|---|
| 1 | ✓ | N/m | 1800 | 1Z | GROUND | 0 | 0 | 0 |
| 2 | ✓ | N/m | 1800 | 2Z | GROUND | 0 | 0 | 0 |
| 3 | ✓ | N/m | 1800 | 3Z | GROUND | 0 | 0 | 0 |
| ... | ... | ... | ... | ... | ... | ... | ... | ... |
| 45 | ✓ | N/m | 1800 | 45Z | GROUND | 0 | 0 | 0 |

Assuming a nodal mass of m = 60 g across all 45 nodes gave a spring rate in the Z direction of $K_z = m\Omega_z^2 = 1800$ N/m. The nodal mass of m = 60 g gave a mass of 2.7 kg (45 times 0.06), which allowed about 0.3 kg for the attachment stem at the base of the blade. Each DOF-to-ground connection was made using the entries in **Table 4**, specifying the use of spring modifications via N/m in column 3, the actual stiffness (spring rate) desired which was 1800 N/m in column 4, the degree of freedom to be stiffened in the Z out-of-plane direction in column 5, the other end of the spring being attached to ground in column 6, and the default values of ground to be (X,Y,Z) = (0,0,0) in columns 7–9. **Table 4** was used to alter the spring matrix created within the STAR7 model.

Spring rates in the Z direction were calculated as $K_z = m\Omega_z^2$ N/m. The Z-axis was chosen for the DOF-to-ground structural dynamics modification because all four modes of vibration consisted of out-of-plane Z-axis motion. **Figure 7** clearly showed that the flapping modes 1, 2, and 4 had their displacements in the Z-direction. Although **Figure 8** showed that the torsion mode-3 rotated about the X-axis, this torsion mode comprised the leading edge of the tail-rotor blade displacing in one Z-axis direction and the trailing edge of the tail-rotor blade displacing in the opposite Z-axis direction. Thus, all four subject modes involved Z-axis motion.

**Table 5** first lists the STAR7 frequency and damping for modes 1–4, at zero

angular velocity, for the first set of test data.

**Table 5.** STAR7 Empirical Modal Frequencies and Damping, $\Omega_z$ = 0 and 173.2 rad/sec.

| STAR7 mode number | Angular velocity $\Omega_z$ | STAR7-ACF frequency ω | STAR7-ACF damping ζ |
|---|---|---|---|
| 1 (Source: Test-1) | 0 | 19.31 Hz | 1.51% |
| 2 (Source: Test-1) | 0 | 110.35 Hz | 5.16% |
| 3 (Source: Test-1) | 0 | 186.43 Hz | 0.19% |
| 4 (Source: Test-1) | 0 | 278.40 Hz | 0.64% |
| 5 (Mode-1+SDM) | 173.2 | 36.13 Hz | 0.82% |
| 6 (Mode-2+SDM) | 173.2 | 117.39 Hz | 4.85% |
| 7 (Mode-3+SDM) | 173.2 | 190.85 Hz | 0.19% |
| 8 (Mode-4+SDM) | 173.2 | 279.92 Hz | 0.64% |

In **Tables 5** and **6**, modes 5–8 are modes 1–4 respectively, stiffened via structural dynamics modification (SDM). This stiffening was accomplished via springs specified in **Table 4** which were designed to simulate centrifugal-stiffening that tended to straighten the helicopter tail-rotor blade and raise modal frequencies when at its operational angular velocity of 173.2 radians per second.

**Table 6.** Flapping and Torsion Frequency Ratios, for $\Omega_z$ = 173.2 vs $\Omega_z$ = 0 rad/sec.

| STAR7 stiffened mode | STAR7 mode shape | STAR7 with SDM $\Omega_z$ = 173.2 | STAR7 stationary $\Omega_z$ = 0 | $\Omega_z$ = 173.2 vs. $\Omega_z$ = 0 ratio | Yoo and Shin ratio, γ = 5.017 [17] | Wright ratio, γ = 5.017 [18] |
|---|---|---|---|---|---|---|
| 5 (mode-1 +SDM) | Flapping | 36.13 Hz | 19.31 Hz | 1.871:1 | 1.839:1 | 1.839:1 |
| 6 (mode-2 +SDM) | Flapping | 117.39 Hz | 110.35 Hz | 1.064:1 | 1.156:1 | 1.156:1 |
| 7 (mode-3 +SDM) | Torsion | 190.85 Hz | 186.43 Hz | 1.024:1 | | |
| 8 (mode-4 +SDM) | Flapping | 279.92 Hz | 278.40 Hz | 1.005:1 | 1.059:1 | |

Lima [16] as well as Yoo and Shin [17] defined the important flapping constant T, which is the reciprocal of the square root used by Blevins [15]. T has the units of seconds.

$$Flapping\ T = \sqrt{\frac{ML^4}{EI}} = \frac{(\lambda_1)^2}{2\pi(19.32Hz)} = 0.028964\ seconds$$

Lima [16] as well as Yoo and Shin [17] then defined the nondimensional rotational velocity used to calculate flapping γ = 5.017, which is the product of T and $\Omega_z$ = 173.2 radians/second.

$$Flapping\ \gamma = T\Omega_Z = 5.017\ (unitless)$$

This nondimensional rotational velocity was critical for calculating the flapping frequency ratios of 1.839:1 (between mode-5 and mode-1) and 1.156:1 (between mode-6 and mode-2) from both Yoo and Shin [17] and Wright, et-al. [18], as represented in column 5 in **Table 6**. The value of 1.839:1 was very close to the STAR7 value of 1.871:1, when comparing mode-5 (mode-1 with SDM) and mode-1 itself. The value of 1.059:1, when comparing mode-8 (mode-4 with SDM) and mode-4 itself, was inferred from **Figure 2** of Yoo and Shin [17].

**Table 6** and **Figure 11** showed that the STAR7 frequency ratios exceeded 1:1 for each of modes 5–8 ($\Omega_z$ = 173.2 rad/sec) with respect to their stationary mode ($\Omega_z$ = 0), indicated centrifugal-stiffening for all four modes. Additionally, these ratios

monotonically-decreased with increasing mode number, as shown by the red line in **Figure 11**, which was expected as increasing mode number was associated with increasing frequency. The STAR7 SDM model slightly exceeded Yoo and Shin [17], and Wright [18] for the first flapping ratio, mode-5: mode-1. However, the STAR7 SDM model was slightly lower than Yoo and Shin [17] as well as Wright [18] for the second flapping ratio, mode-6: mode-2. Lastly, the STAR7 SDM model was slightly lower than Yoo and Shin [17] for the third flapping ratio, mode-8: mode-4. The =PEARSON correlation between the STAR7 frequency ratios in column 4 of **Table 6** and the Yun and Shin frequency ratios in column 5 was 99.857% with the sum of the square of the errors equaling 0.012404, indicating a very strong correlation between our centrifugally-stiffened tail-rotor blade and a centrifugally-stiffened Euler-Bernoulli beam.

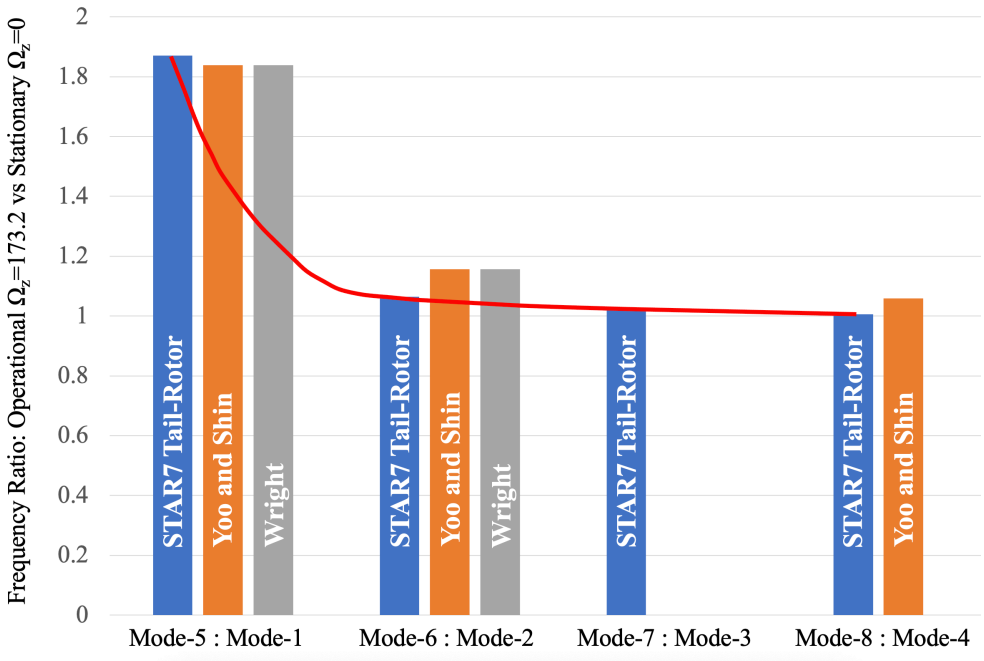


**Figure 11.** Frequency Ratio: Operational ($\Omega_z$ = 173.2) versus Stationary ($\Omega_z$ = 0).

The red line depicting the monotonically-decreasing ratio of centrifugal stiffening of STAR7 mode$_i$ in **Figure 11** was approximated by the following equation. The decrease in centrifugal stiffening ratio with increasing modal frequency is a necessary result of modal energies. The amplitude of higher modes of vibration has to be smaller than lower modes, or the modal energies will grow with frequency. This lower the modal amplitude with increasing modal frequency means that there will be less centrifugal stiffening for the higher modes of vibration.

$$Ratio\ of\ Centrifugal\ Stiffening\ of\ STAR7\ Mode_i = 1 + 0.871\left[\frac{\omega_1}{\omega_i}\right]^{1.547}$$

This equation had an =PEARSON correlation of 99.83% with the ratio of $\Omega_z$ = 173.2 versus $\Omega_z$ = 0, column 5 of **Table 6**. The sum of the square of the errors between the above equation and the respective STAR7 mode ratios was 0.000103471.

### 4.3. STAR7 combined modal assurance criterion, $\Omega_z = 0$ and 173.2 rad/sec

**Figure 12** shows a 3-D histogram (left) and a 2-D table (right) Modal Assurance Criterion for $\Omega_z = 0$ (modes 1–4) and $\Omega_z = 173.2$ rad/sec (modes 5–8, which are modes 1–4 with structural dynamics modification). Auxiliary thick black lines, superimposed on the 8-by-8 MAC table, partitioned it into four 4-by-4 quadrants. The upper left-quadrant of the 2-D table MAC in **Figure 12** represents the apples-to-apples comparison of modes 1–4 for zero angular velocity, $\Omega_z = 0$, as previously shown separately in **Figure 9**. The lower right-quadrant of the 2-D table MAC in **Figure 12** is the apples-to-apples comparison of modes 5–8, where modes 1–4 now experience an operational angular velocity of $\Omega_z = 173.2$ radians per second. Both the upper-left and the lower-right quadrants are symmetric, and the purple main diagonal which they form has values of 100% for an autocorrelation, as expected. The lower-left and the upper right quadrants of the 2-D table MAC in **Figure 12** are apples-to-oranges comparisons of modes 1–4 versus modes 5–8. The lower-left and the upper right quadrants are not themselves symmetric about their respective subdiagonals; however, these two quadrants are mirror-images of each other about the main diagonal of **Figure 12**. Thus, the overall 8-by-8 MAC in **Figure 12** is a symmetric matrix, as desired.

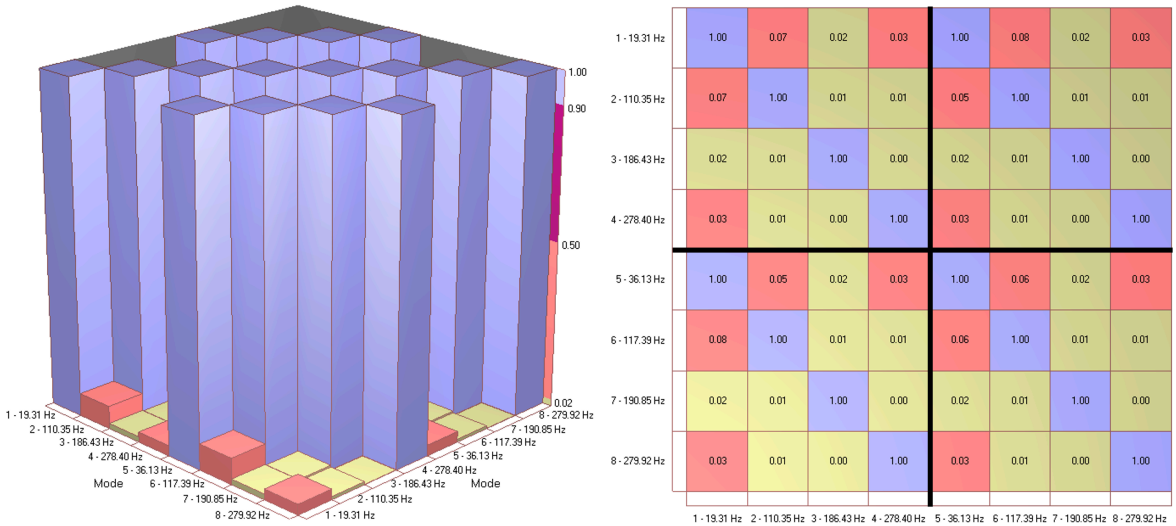


**Figure 12.** 3-D (left) and 2-D (right) Modal Assurance Criterion, $\Omega_z = 0$ and 173.2 rad/sec.

Additionally, the purple subdiagonals in the lower-left and the upper right quadrants of the 2-D table MAC showed 100% correlations, indicating that the mode shapes in **Figures 7** and **8** were not meaningfully affected between the stationary angular velocity of $\Omega_z = 0$ and the operational angular velocity of $\Omega_z = 173.2$ radians per second. Yoo and Shin [17] did report shifts in mode shape, but at the nondimensional rotational velocity of $\gamma = 50$, which was an order of magnitude greater than our value of $\gamma = 5.017$.

## 5. Conclusion

The three flapping modes of the stationary tail-rotor blade, as well as the centrifugal-stiffening of these flapping modes, of our digital-twin compared favorably with Euler-Bernoulli beam theory, with cross-correlations varying favorably between

99.83%–99.9%. The orthogonality of the flapping and torsional modes was demonstrated via the Modal Assurance Criterion, with cross-correlations varying favorably between 0% to 8%. This information was used to understand that flapping mode-1, which had the highest amplitude of out-of-plane vibration, also experienced the most centrifugal stiffening. As the modal frequencies increased, the amplitude of out-of-plane vibration decreased, resulting in increasingly less centrifugal stiffening. This stiffening was expressed in equation form with a cross-correlation of 99.83%. Thus, the accuracy of our digital-twin approach was confirmed.

**Author contributions:** Conceptualization, KL and DW; methodology, DW; validation, ML, DW and TW; formal analysis, ML, DW and TW; investigation, KL., DW and TW; writing—original draft preparation, DW; writing—review and editing, ML, KL, DW and TW; visualization, KL and DW; supervision, KL; project administration, KL and DW. All authors have read and agreed to the published version of the manuscript.

**Funding:** This research received no external funding.

**Acknowledgment:** Donna Robinson Winarski is acknowledged for her support of this research.

**Conflict of interest:** The authors declare no conflict of interest.

## Abbreviation

| | |
|---|---|
| *.CMM | Spectral Dynamics STAR7 model file |
| *.CRD | Coordinates file (Structural Measurements System SMS StarStruct) |
| *.FRF | Frequency Response Function file (SMS StarStruct) |
| *.PRJ | Project file (STAR7) |
| *.RST | ANSYS Finite Element Re-Structured Text mode-shape file |
| *.SDD | Spectral Dynamics Data file (STAR7) |
| *.SWS | STAR7 workspace file |
| ACF | Advanced Curve Fitter Method (STAR7) |
| B&K | Brüel & Kjær, as of 2019 now called HBK (Hottinger Brüel & Kjær) |
| F&D | Frequency and Damping |
| EI | Flexural Rigidity |
| IFFT | Inverse Fast Fourier Transform |
| $K_z$ | STAR7 SDM Stiffness addition, spring rate in the Z direction |
| L | Length of Tail-Rotor Blade, 1.16m |
| LSCE | Least Square Complex Exponential |
| m | Nodal Mass attributed individually to each of the 45 nodes |
| M | Mass per unit length of Tail-Rotor Blade |
| MAC | Modal Assurance Criterion, either a 3-D histogram or a 2-D table |
| MIF | Mode Indicator Function (STAR7) |
| R | Arc of the tip of Tail-Rotor, 1.295m |
| SDM | Structural Dynamics Modification |
| T | Flapping vibrational constant, with units of seconds |
| $\gamma$ | Nondimensional rotational velocity, $\gamma = T\Omega_z$ |
| $\zeta$ | Modal Damping Ratio, in Percent |
| $\lambda$ | Solutions to the transcendental equation $\cos(\lambda)\cosh(\lambda) + 1 = 0$ |

| | |
|---|---|
| $\omega$ | Modal Vibration Frequency, in Hertz |
| $\Omega_z$ | Angular velocity in rad/sec of the Tail-Rotor Blade about the Z-axis |

## References


1. Bell UH-1 Iroquois helicopter. Available online: https://en.wikipedia.org/wiki/Bell_UH-1_Iroquois (accessed on 17 July 2025).
2. By airwolfhound from hertfordshire, UK-UH1 Huey-Fly Navy 2017, CC BY-SA 2.0. Available online: https://commons.wikimedia.org/w/index.php?curid=69215127 (accessed on 19 July 2025).
3. Guivarch D, Mermoz E, Marino Y, et al. Creation of helicopter dynamic systems digital twin using multibody simulations. CIRP Annals. 2019; 68(1): 133–136. doi: 10.1016/j.cirp.2019.04.041
4. Li L, Aslam S, Wileman A, et al. Digital twin in aerospace industry: a gentle introduction. IEEE Access. 2022; 10: 9543–9562. doi: 10.1109/ACCESS.2021.3136458
5. Santos FLM, Peeters B, Van der Auweraer H, et al. Experimental damage detection of a helicopter main rotor blade based on modal properties. In: Proceedings of the International conference on engineering structural dynamics ICEDyn-2013, Sesimbra, Portugal, 17 June 2013. Available online: https://www.researchgate.net/publication/278963286_EXPERIMENTAL_DAMAGE_DETECTION_OF_A_HELICOPTER_MAIN_ROTOR_BLADE_BASED_ON_MODAL_PROPERTIES
6. Grappasonni C, Ameri N, Giuliano C, et al. Dynamic identification of helicopter structures using operational modal analysis methods in the presence of harmonic loading. In: Proceedings of the 25th International Conference on Noise and Vibration engineering (ISMA2012), Leuven, Belgium, 17 September 2012. Available online: https://past.isma-isaac.be/downloads/isma2012/papers/isma2012_0363.pdf
7. Rizo-Patron S, Sirohi J. Operational modal analysis of a helicopter rotor blade using digital image correlation. Experimental Mechanics. 2017; 57(3): 367–375. doi: 10.1007/s11340-016-0230-6
8. Bell UH-1H and UH-1C Iroquois (Huey) Tail-Rotors, on display at Pima Air and Space Museum, Tucson, Arizona. Available online: https://pimaair.org (accessed on 24 July 2025).
9. Product Data: Piezoelectric Charge Accelerometer Types 4393 and 4393-V. Available online: https://www.bksv.com/media/doc/bp2043.pdf (accessed on 30 July 2023).
10. Product Data: Impact Hammer Type 8202. Available online: https://www.scribd.com/document/466383040/Bp0385-pdf (accessed on 30 July 2023).
11. Serridge M, Licht T. Piezoelectric Accelerometers and Vibration Preamplifiers: Theory and Application Handbook. Brüel & Kjær; 1987. Available online: https://www.bksv.com/media/doc/bb0694.pdf (accessed on 30 July 2023).
12. Winarski D, Nygren KP, Winarski T. Modes of vibration in basketball rims and backboards and the energy rebound testing device. Vibration. 2023; 6(4): 726–742. doi: 10.3390/vibration6040045
13. CATS: Computer aided test suite dynamic control and analysis STAR 7 advanced modal analysis. Available online: https://www.scribd.com/document/394925642/665498-MATERIJALI-1-Skripta-Listopad-2013 (accessed on 10 June 2023).
14. ANSYS 2025 R2 student edition software package. Available online: https://www.ansys.com/academic/students/ansys-student (accessed on 30 August 2025).
15. Blevins RD. Formulas for natural frequency and mode shape. Krieger Publishing; 2001. p. 108.
16. Lima MACF. Rotating cantilever beams: finite element modeling and vibration analysis [Master's Thesis]. Universidade do Porto; 2012. Available online: https://repositorio-aberto.up.pt/bitstream/10216/68449/1/000154284.pdf
17. Yoo HH, Shin SH. Vibration analysis of rotating cantilever beams. Journal of Sound and Vibration. 1998; 212(5): 807–828. doi: 10.1006/jsvi.1997.1469
18. Wright AD, Smith CE, Thresher RW, et al. Vibration modes of centrifugally stiffened beams. Journal of Applied Mechanics. 1982; 49(1): 197–202. doi: 10.1115/1.3161966
19. STAR7 Operating Manual, Rev. 1b, Supplied to STAR7 customers of Spectral Dynamics. Spectral Dynamics, Inc: San Jose, CA, USA.
20. Pastor M, Binda M, Harčarik T. Modal assurance criterion. Procedia Engineering. 2012; 48: 543–548. doi: 10.1016/j.proeng.2012.09.551
21. Greś S, Döhler M, Mevel L. Uncertainty quantification of the Modal Assurance Criterion in operational modal analysis. Mechanical Systems and Signal Processing. 2021; 152: 107457. doi: 10.1016/j.ymssp.2020.107457
22. Allemang RJ. The modal assurance criterion–twenty years of use and abuse. Sound and vibration. 2003; 37(8): 14–23. Available online: http://www.sandv.com/downloads/0308alle.pdf
23. Samman MM. A modal correlation coefficient for detection of kinks in mode shapes. Journal of Vibration and Acoustics. 1996; 118(2): 271–272. doi: 10.1115/1.2889658
24. Brehm M, Zabel V, Bucher C. An automatic mode pairing strategy using an enhanced modal assurance criterion based on modal strain energies. Journal of Sound and Vibration. 2010; 329(25): 5375–5392. doi: 10.1016/j.jsv.2010.07.006
25. Fotsch D, Ewins DJ. Application of MAC in the frequency domain. In: Proceedings of SPIE—The International Society for Optical Engineering. SPIE; 2000. pp. 1225–1231. Available online: https://www.researchgate.net/publication/2526990_Application_Of_Mac_In_The_Frequency_Domain